

Integrating Photonics into Fab Labs

Adam, Aurele

Publication date

2018

Document Version

Final published version

Published in

Optics & Photonics News

Citation (APA)

Adam, A. (2018). Integrating Photonics into Fab Labs. *Optics & Photonics News*, 29(9), 22-24.
https://www.osa-opn.org/home/articles/volume_29/september_2018/departments/integrating_photonics_into_fab_labs/

Important note

To cite this publication, please use the final published version (if applicable).
Please check the document version above.

Copyright

Other than for strictly personal use, it is not permitted to download, forward or distribute the text or part of it, without the consent of the author(s) and/or copyright holder(s), unless the work is under an open content license such as Creative Commons.

Takedown policy

Please contact us and provide details if you believe this document breaches copyrights.
We will remove access to the work immediately and investigate your claim.

Green Open Access added to TU Delft Institutional Repository

'You share, we take care!' – Taverne project

<https://www.openaccess.nl/en/you-share-we-take-care>

Otherwise as indicated in the copyright section: the publisher is the copyright holder of this work and the author uses the Dutch legislation to make this work public.

Multi-parameter inversion with the aid of particle velocity field reconstruction

Ulas Taskin^{1, a)} and Koen W. A. van Dongen¹

*Department of Imaging Physics, Delft University of Technology, Delft, 2628CJ,
the Netherlands.*

(Dated: 27 July 2020)

1 Multi-parameter inversion for medical ultrasound leads to an improved tissue clas-
2 sification. In general, simultaneous reconstruction of volume density of mass and
3 compressibility would require knowledge of the particle velocity field alongside with
4 the pressure field. However, in practice the particle velocity field is not measured.
5 Here, we propose a method for multi-parameter inversion where the particle velocity
6 field is reconstructed from the measured pressure field. To this end, the measured
7 pressure field is described using outward propagating Hankel functions. For a syn-
8 thetic setup, it is shown that the reconstructed particle velocity field matches the
9 forward modelled particle velocity field. Next, the reconstructed particle velocity
10 field is used together with the synthetically measured pressure field to reconstruct
11 density and compressibility profiles with the aid of contrast source inversion (CSI).
12 Finally, comparing the reconstructed speed of sound profiles obtained via single-
13 parameter versus multi-parameter inversion shows that multi-parameter outperforms
14 single-parameter inversion with respect to accuracy and stability.

^{a)}u.taskin@tudelft.nl; Department of Imaging Physics, Delft University of Technology, Delft, 2628CJ, the Netherlands.

15 I. INTRODUCTION

16 Ultrasound is widely used as a medical imaging modality due to its features such as being
17 non-invasive and safe. To retrieve quantitative information about the tissues in the image,
18 ultrasound tomography¹⁻³ in combination with full-wave inversion⁴⁻⁷ is frequently used. Up
19 to date, these methods are successfully applied in cases where the object is surrounded by
20 transducers. Examples are the breast⁸, brain⁹ and bone¹⁰.

21 Most inversion methods aim for speed of sound reconstruction by assuming constant mass
22 density. This is mainly done to simplify the complex non-linear inverse problem. However,
23 quantitative knowledge about multiple medium parameters may lead to an improved tissue
24 characterization¹¹.

25 In various recent works, full-wave inversion is used for multi-parameter reconstruction.
26 For example, contrast source inversion (CSI) and Born iterative method (BIM) are used to
27 reconstruct compressibility, attenuation and density^{12,13}. In these works the parameters are
28 directly reconstructed from the pressure field measurements. However, with these methods
29 additional regularization is needed to reconstruct the density accurately¹⁴. Alternatively,
30 the particle velocity field is used together with the pressure field to reconstruct density and
31 compressibility simultaneously using a full vectorial CSI scheme¹⁵. Unfortunately, in practice
32 only the pressure field is measured and the particle velocity field is unknown. Therefore, full
33 vectorial CSI method can not be used directly in practical applications.

34 In this work, we propose a multi-parameter inversion method where we first reconstruct
35 the particle velocity field from the pressure field measured on a closed arbitrary-shaped

36 two-dimensional (2-D) curvature. The particle velocity field reconstruction method is based
 37 on Hankel function decomposition of the measured pressure field¹⁶. Once the pressure field
 38 is expressed with Hankel functions, the particle velocity field is computed by applying the
 39 gradient operator to the derived expression. After a successful reconstruction of the particle
 40 velocity field from the pressure field, both the compressibility and the mass density are
 41 reconstructed using a vectorial CSI scheme¹⁵.

42 The paper is organized as follows: Section II presents the forward model, the method to
 43 reconstruct the particle velocity field from the pressure field and finally the inverse problem.
 44 Section III presents numerical examples in which the reconstructed particle velocity field is
 45 compared with the ground truth. In addition, reconstructed density, compressibility and
 46 speed of sound profiles are presented. These profiles are obtained by employing CSI on the
 47 measured pressure and reconstructed particle velocity field. Finally, conclusions are given
 48 in Section IV.

49 II. THEORY

50 Consider an arbitrary-shaped object with unknown medium properties within the spatial
 51 domain \mathbb{D} enclosed by the boundary \mathbb{S} . The sources and receivers are located on the boundary
 52 \mathbb{S} , see Fig. 1. The boundary \mathbb{S} is located in the homogeneous lossless embedding with
 53 speed of sound c_0 , volume density of mass ρ_0 and compressibility κ_0 . The object domain
 54 is heterogeneous in all three medium parameters. The Cartesian and polar position vectors
 55 are denoted by $\mathbf{x} = (x, y)$ and $\mathbf{r} = (r, \phi)$ respectively. The following theory is presented in
 56 the temporal Fourier domain with angular frequency ω .

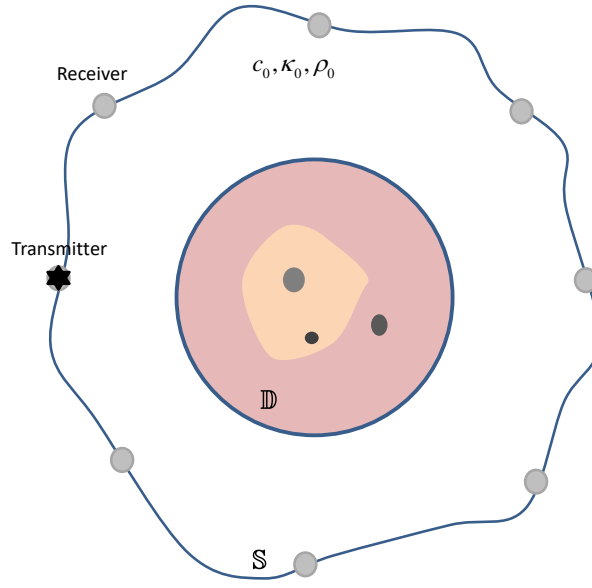


FIG. 1. Schematic representation of the setup. Transmitters and receivers are located in \mathbb{S} . \mathbb{S} encloses the object within the domain \mathbb{D} .

57 A. Forward Problem

58 The acoustic field equations are given by the equation of motion and deformation. In the
 59 temporal Fourier domain these equations read^{17,18}

$$\nabla \hat{p}(\mathbf{x}) + j\omega\rho(\mathbf{x})\hat{\mathbf{v}}(\mathbf{x}) = \hat{\mathbf{f}}(\mathbf{x}) \quad (1)$$

60 and

$$\nabla \cdot \hat{\mathbf{v}}(\mathbf{x}) + j\omega\kappa(\mathbf{x})\hat{p}(\mathbf{x}) = \hat{q}(\mathbf{x}), \quad (2)$$

61 where $\hat{p}(\mathbf{x})$ is the pressure wave field, $\hat{\mathbf{v}}(\mathbf{x})$ is the particle velocity wave field, $\rho(\mathbf{x})$ is the
 62 volume density of mass, $\kappa(\mathbf{x})$ is the compressibility, $\hat{\mathbf{f}}(\mathbf{x})$ is the volume source density of
 63 volume force, $\hat{q}(\mathbf{x})$ is the volume source density of injection rate, j is the imaginary number
 64 defined via the relation $j^2 = -1$, and ∇ is the nabla operator. The caret symbol $\hat{}$ is used

65 for quantities defined in the temporal Fourier domain. The incident wave fields $\hat{p}^{inc}(\mathbf{x})$ and
 66 $\hat{\mathbf{v}}^{inc}(\mathbf{x})$ are defined as the wave fields that are generated by the primary sources $\hat{q}(\mathbf{x})$ and
 67 $\hat{\mathbf{f}}(\mathbf{x})$, and that propagate in the homogeneous embedding in the absence of any acoustic
 68 contrast. In view of this definition, the scattered wave fields $\hat{p}^{sct}(\mathbf{x})$ and $\hat{\mathbf{v}}^{sct}(\mathbf{x})$ are defined
 69 as the numerical difference between the actual or total wave fields $\hat{p}(\mathbf{x})$ and $\hat{\mathbf{v}}(\mathbf{x})$, and the
 70 incident wave fields $\hat{p}^{inc}(\mathbf{x})$ and $\hat{\mathbf{v}}^{inc}(\mathbf{x})$. The scattered fields can be written in integral form
 71 as^{17,18}

$$\begin{aligned} \hat{p}^{sct}(\mathbf{x}) = \hat{p}(\mathbf{x}) - \hat{p}^{inc}(\mathbf{x}) = & \frac{\omega^2}{c_0^2} \int_{\mathbf{x}' \in \mathbb{D}} \hat{G}(\mathbf{x} - \mathbf{x}') \chi^\kappa(\mathbf{x}') \hat{p}(\mathbf{x}') dV(\mathbf{x}') \\ & + j\omega\rho_0 \nabla \cdot \int_{\mathbf{x}' \in \mathbb{D}} \hat{G}(\mathbf{x} - \mathbf{x}') \chi^\rho(\mathbf{x}') \hat{\mathbf{v}}(\mathbf{x}') dV(\mathbf{x}') \end{aligned} \quad (3)$$

72 and

$$\begin{aligned} \hat{\mathbf{v}}^{sct}(\mathbf{x}) = \hat{\mathbf{v}}(\mathbf{x}) - \hat{\mathbf{v}}^{inc}(\mathbf{x}) = & j\omega\kappa_0 \nabla \int_{\mathbf{x}' \in \mathbb{D}} \hat{G}(\mathbf{x} - \mathbf{x}') \chi^\kappa(\mathbf{x}') \hat{p}(\mathbf{x}') dV(\mathbf{x}') \\ & - \nabla \nabla \cdot \int_{\mathbf{x}' \in \mathbb{D}} \hat{G}(\mathbf{x} - \mathbf{x}') \chi^\rho(\mathbf{x}') \hat{\mathbf{v}}(\mathbf{x}') dV(\mathbf{x}') - \chi^\rho(\mathbf{x}) \hat{\mathbf{v}}(\mathbf{x}), \end{aligned} \quad (4)$$

73 where $\hat{G}(\mathbf{x} - \mathbf{x}')$ is the Green's function describing the impulse response of the homogeneous
 74 embedding. The Green's function in 2-D equals

$$\hat{G}(\mathbf{x} - \mathbf{x}') = \frac{i}{4} H_0^{(1)}(k_0 |\mathbf{x} - \mathbf{x}'|) \quad (5)$$

75 where $H_0^{(1)}$ is the zero-order Hankel function of the first kind. The contrast functions $\chi^\kappa(\mathbf{x})$
 76 and $\chi^\rho(\mathbf{x})$ are defined as

$$\chi^\kappa(\mathbf{x}) = \frac{\kappa(\mathbf{x}) - \kappa_0}{\kappa_0} \quad (6)$$

77 and

$$\chi^\rho(\mathbf{x}) = \frac{\rho(\mathbf{x}) - \rho_0}{\rho_0}. \quad (7)$$

78 Eqs. (3) and (4) can be solved numerically for known sources and known contrast functions
 79 to find the unknown total wave fields inside the spatial domain \mathbb{D} . In literature, this situation
 80 is referred to as the forward problem. The situation where the sources generating the wave
 81 fields as well as the total wave fields at the boundary \mathbb{S} are known, and where both the
 82 total wave fields and the contrast functions are unknown within the domain of interest \mathbb{D} is
 83 referred to as the inverse problem. Unfortunately, in practice one only measures the pressure
 84 field and not the particle velocity field. In the next section we present a method that allows
 85 us to reconstruct the particle velocity field from the measured pressure field.

86 B. particle Velocity Field Reconstruction

87 Multi-parameter inversion requires knowledge of both the pressure and particle velocity
 88 wave fields, where the latter one is not measured in practice. Here we present a method to
 89 construct the particle velocity field from pressure field measurements.

90 The scattered field satisfies the 2-D Helmholtz equation, which reads in polar coordinates

91

$$r^2 \frac{\partial^2 \hat{p}^{sct}(\mathbf{r})}{\partial r^2} + r \frac{\partial \hat{p}^{sct}(\mathbf{r})}{\partial r} + \frac{\partial^2 \hat{p}^{sct}(\mathbf{r})}{\partial \phi^2} + r^2 \frac{\omega^2}{c^2(\mathbf{r})} \hat{p}^{sct}(\mathbf{r}) = 0. \quad (8)$$

92 Under the condition that the solution of Eq. (8) represents an outward propagating wave
 93 field at the boundary of \mathbb{S} , the resulting scattered field may be formulated as¹⁶

$$\hat{p}^{sct}(\mathbf{r}) = \sum_{n=-N}^N \hat{c}_n H_n^{(1)}\left(\frac{\omega}{c_0} r\right) e^{jn\phi}, \quad (9)$$

94 where $H_n^{(1)}\left(\frac{\omega}{c_0} r\right)$ are Hankel functions of the first kind and order n representing the outward
 95 propagating waves¹⁹. To find the complex valued coefficients \hat{c}_n for each angular frequency

96 ω , Eq. (9) is solved for \hat{c}_n using the known scattered pressure field $\hat{p}^{sct}(\mathbf{r})$ measured on
 97 \mathbb{S}^{16} . Once the coefficients \hat{c}_n are reconstructed, the scattered particle velocity field $\hat{\mathbf{v}}^{sct}(\mathbf{r})$ is
 98 computed by considering the gradient of the scattered pressure field, hence

$$\hat{\mathbf{v}}^{sct}(\mathbf{r}) = -\frac{1}{j\omega\rho_0}\nabla\hat{p}^{sct}(\mathbf{r}). \quad (10)$$

99 By combining Eqs. (9) and (10) the following expressions for the particle velocity field in
 100 cylindrical coordinates $\hat{\mathbf{v}}^{sct}(\mathbf{r}) = (\hat{v}_r^{sct}(\mathbf{r}), \hat{v}_\phi^{sct}(\mathbf{r}))$ are obtained

$$\begin{aligned} \hat{v}_r^{sct}(\mathbf{r}) &= -\frac{1}{j\omega\rho_0}\frac{\partial\hat{p}^{sct}(\mathbf{r})}{\partial r} \\ &= -\frac{1}{j\omega\rho_0}\times\sum_{n=-N}^N\left[H_{n-1}^{(1)}\left(\frac{\omega}{c_0}r\right)-H_{n+1}^{(1)}\left(\frac{\omega}{c_0}r\right)\right]\hat{c}_n\frac{\omega}{2c_0}e^{jn\phi} \end{aligned} \quad (11)$$

101 and

$$\hat{v}_\phi^{sct}(\mathbf{r}) = -\frac{1}{j\omega\rho_0}\frac{\partial\hat{p}^{sct}(\mathbf{r})}{\partial\phi} = -\frac{1}{j\omega\rho_0}\times\sum_{n=-N}^Njn\hat{c}_nH_n^{(1)}\left(\frac{\omega}{c_0}r\right)e^{jn\phi}, \quad (12)$$

102 where we use recurrence relations to compute the spatial derivatives of the Hankel func-
 103 tions²⁰.

104 C. Inverse Problem

105 Full-wave inversion methods aim to reconstruct medium parameters by iteratively mini-
 106 mizing a cost function. Typically, this cost function contains at least one term that shows
 107 a measure for the mismatch between the measured and the modelled wave fields. A well-
 108 known full-wave inversion method is CSI. This method can be implemented such that it
 109 reconstructs multiple medium parameters simultaneously¹⁵.

110 **1. Multi-parameter inversion**

111 Employing CSI for a multi-parameter inverse problem requires the formulation of the
 112 following cost functional

$$\text{Err}^{(1)} = \eta_{\mathbb{S}}^{pv} \left\| \begin{array}{c} \mathbf{p}^{sct} - \mathbf{L}_p^{\mathbb{S}}[\mathbf{w}^\kappa, \mathbf{w}^\rho] \\ \mathbf{v}^{sct} - \mathbf{L}_v^{\mathbb{S}}[\mathbf{w}^\kappa, \mathbf{w}^\rho] \end{array} \right\|_{\mathbb{S}}^2 + \eta_{\mathbb{D}}^{pv} \left\| \begin{array}{c} \chi^\kappa \mathbf{p}^{inc} + \chi^\kappa \mathbf{L}_p^{\mathbb{D}}[\mathbf{w}^\kappa, \mathbf{w}^\rho] - \mathbf{w}^\kappa \\ \chi^\rho \mathbf{v}^{inc} + \chi^\rho \mathbf{L}_v^{\mathbb{D}}[\mathbf{w}^\kappa, \mathbf{w}^\rho] - \mathbf{w}^\rho \end{array} \right\|_{\mathbb{D}}^2, \quad (13)$$

113 where $\eta_{\mathbb{S}}^{pv}$ and $\eta_{\mathbb{D}}^{pv}$ are normalization terms, $\mathbf{L}_p^{\mathbb{S}}$, $\mathbf{L}_p^{\mathbb{D}}$, $\mathbf{L}_v^{\mathbb{S}}$ and $\mathbf{L}_v^{\mathbb{D}}$ are integral operators that
 114 map the contrast sources \mathbf{w}^κ and \mathbf{w}^ρ to the pressure and particle velocity wave fields in \mathbb{S}
 115 and \mathbb{D} , and where $\|\cdot\|_{\mathbb{S}}$ and $\|\cdot\|_{\mathbb{D}}$ represent the l_2 -norm of a quantity defined in \mathbb{S} and \mathbb{D}
 116 respectively. For a spatially varying compressibility and density the contrast sources equal

$$\mathbf{w}^\kappa = \chi^\kappa \mathbf{p} \quad (14)$$

117 and

$$\mathbf{w}^\rho = \chi^\rho \mathbf{v}. \quad (15)$$

118 To solve the inverse problem for the unknown contrast functions χ^κ and χ^ρ , the cost function
 119 in Eq. (13) is minimized iteratively for known incident fields in \mathbb{S} and \mathbb{D} and scattered fields
 120 in \mathbb{S} .

121 **2. Single-parameter inversion**

122 It is common practice to assume a constant density throughout the entire domain, i.e.
 123 $\rho(\mathbf{r}) = \rho_0$. Within this assumption the vectorial problem reduces to a scalar problem and

124 the cost function $\text{Err}^{(1)}$ for CSI that needs to be minimized reduces to,²¹

$$\text{Err}^{(2)} = \eta_{\mathbb{S}} \left\| \mathbf{p}^{\text{sct}} - \mathbf{L}_p^{\mathbb{S}}[\mathbf{w}^{\kappa}] \right\|_{\mathbb{S}}^2 + \eta_{\mathbb{D}} \left\| \boldsymbol{\chi}^{\kappa} \mathbf{p}^{\text{inc}} - \mathbf{w}^{\kappa} - \boldsymbol{\chi}^{\kappa} \mathbf{L}_p^{\mathbb{D}}[\mathbf{w}^{\kappa}] \right\|_{\mathbb{D}}^2. \quad (16)$$

125 Note that, for this single-parameter inversion a spatially varying speed of sound profile is
 126 obtained via the relation $c(\mathbf{x}) = \frac{1}{\sqrt{\kappa(\mathbf{x})\rho_0}}$.

127 III. RESULTS

128 A synthetic example is presented in this section. First, the forward problem is solved
 129 to obtain both pressure and particle velocity fields²². Next, the particle velocity field is
 130 computed with the proposed method and compared with the “exact” result obtained by
 131 directly solving the forward problem. Finally, contrasts source inversion (CSI) is used as a
 132 multi- and single-parameter inversion method.

133 A. Configuration

134 A synthetic “breast” phantom is used in this work. The phantom alongside with the
 135 transducer locations is shown in Fig. 2. The medium parameters of the tissues are listed in
 136 Table I^{23,24}. Attenuation is neglected since it is known to have little effect on the acoustic
 137 fields at these frequencies²⁵. The spatial domain contains 100×100 elements of size $0.42 \text{ mm} \times$
 138 0.42 mm . The 32 sources and 128 receivers are equally distributed over the white dotted
 139 circle indicating \mathbb{S} (see Fig. 2)²⁶. In Fig. 3, the source excitation is given; a Gaussian
 140 modulated pulse with a center frequency $f_0 = 0.2 \text{ MHz}$.

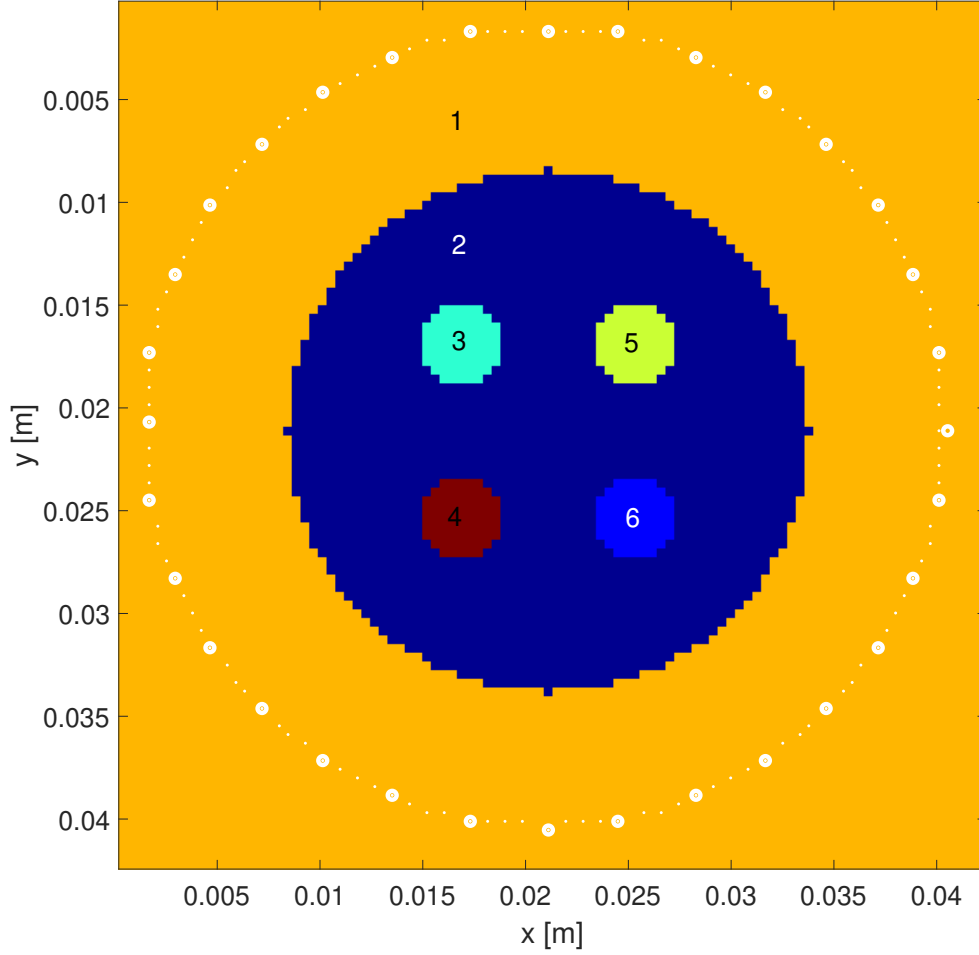


FIG. 2. Synthetic breast phantom. The large and small white dots show the locations of the sources and the receivers respectively. The numbers indicate the different tissue types.

141 B. Solution of Forward Problem

142 Synthetic data (both pressure and particle velocity field) is obtained by solving the for-
 143 ward problem for the breast phantom in the frequency domain²². Time-domain results are
 144 obtained using inverse Fourier transformations.

145 Fig. 4 shows snapshots of the incident, scattered and total pressure and particle velocity
 146 fields at $t = 28 \mu\text{s}$. The source is located at $(x, y) = (21 \text{ mm}, 41 \text{ mm})$. The wave fields are

TABLE I. Medium parameters of the tissues.

<i>Tissue #</i>	c [m/s]	ρ [kg/m ³]	κ [1/Pa]
1	1520	996	0.435e-9
2	1494	1013	0.442e-9
3	1514	986	0.442e-9
4	1527	986	0.435e-9
5	1514	1013	0.430e-9
6	1494	1041	0.430e-9

147 computed by solving the full-wave forward problem for the pressure and particle velocity
 148 field simultaneously. The obtained particle velocity field will serve as a benchmark for the
 149 reconstructed particle velocity field.

150 C. particle Velocity Field Reconstruction

151 The particle velocity fields are reconstructed from the pressure fields using the proposed
 152 method. These pressure fields are synthetically measured by the 128 receivers indicated by
 153 the small white dots in Fig. 2 and a single source that is located at $(x, y) = (41 \text{ mm}, 21 \text{ mm})$.

154 First, frequency-domain results are shown in Fig. 5. The top row shows the pressure
 155 fields measured in the receiver locations; in blue the synthetically generated and in red
 156 the reconstructed pressure fields. The following rows show the particle velocity fields. It

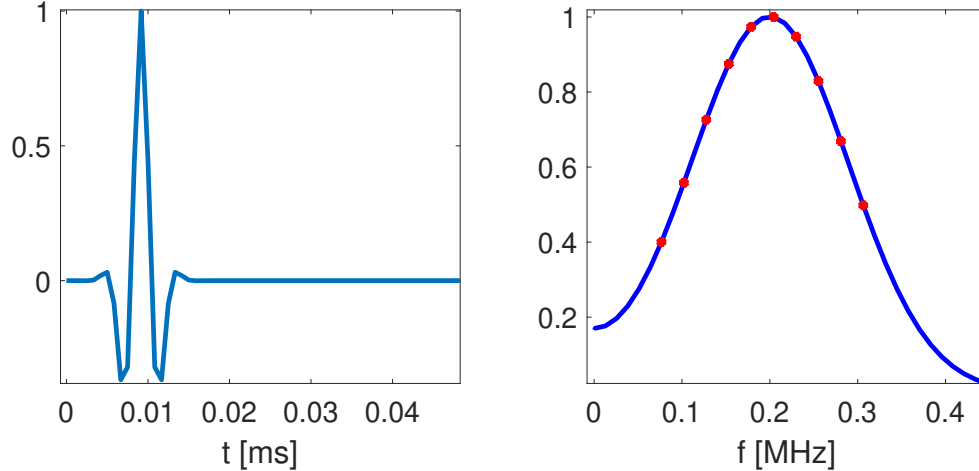


FIG. 3. Excitation profile in time (left) and frequency (right) domain. Red dots indicate the frequency components used with CSI.

157 is seen from these results that the reconstructed fields have an excellent match with the
 158 synthetically generated fields for both amplitude and phase.

159 Next, time-domain results are shown in Fig. 6. The source and receiver locations are given
 160 in the image at the top. A-scans at the given receiver locations for the particle velocity field
 161 are given in the bottom images. Ground truth and reconstructed fields are plotted together.
 162 These results show that the proposed method works well over the entire bandwidth.

163 D. Solution of Inverse Problem

164 The effect of the particle velocity field on the inversion is shown in this subsection. First,
 165 contrast source inversion (CSI) is used in its traditional way²⁷ by using only the pressure
 166 field and inverting for the speed of sound (assuming constant density) only. Note that, the
 167 forward problem is based on a spatially varying compressibility as well as density profile.
 168 Next, CSI is used as described in Ref. 15 by using pressure and particle velocity fields

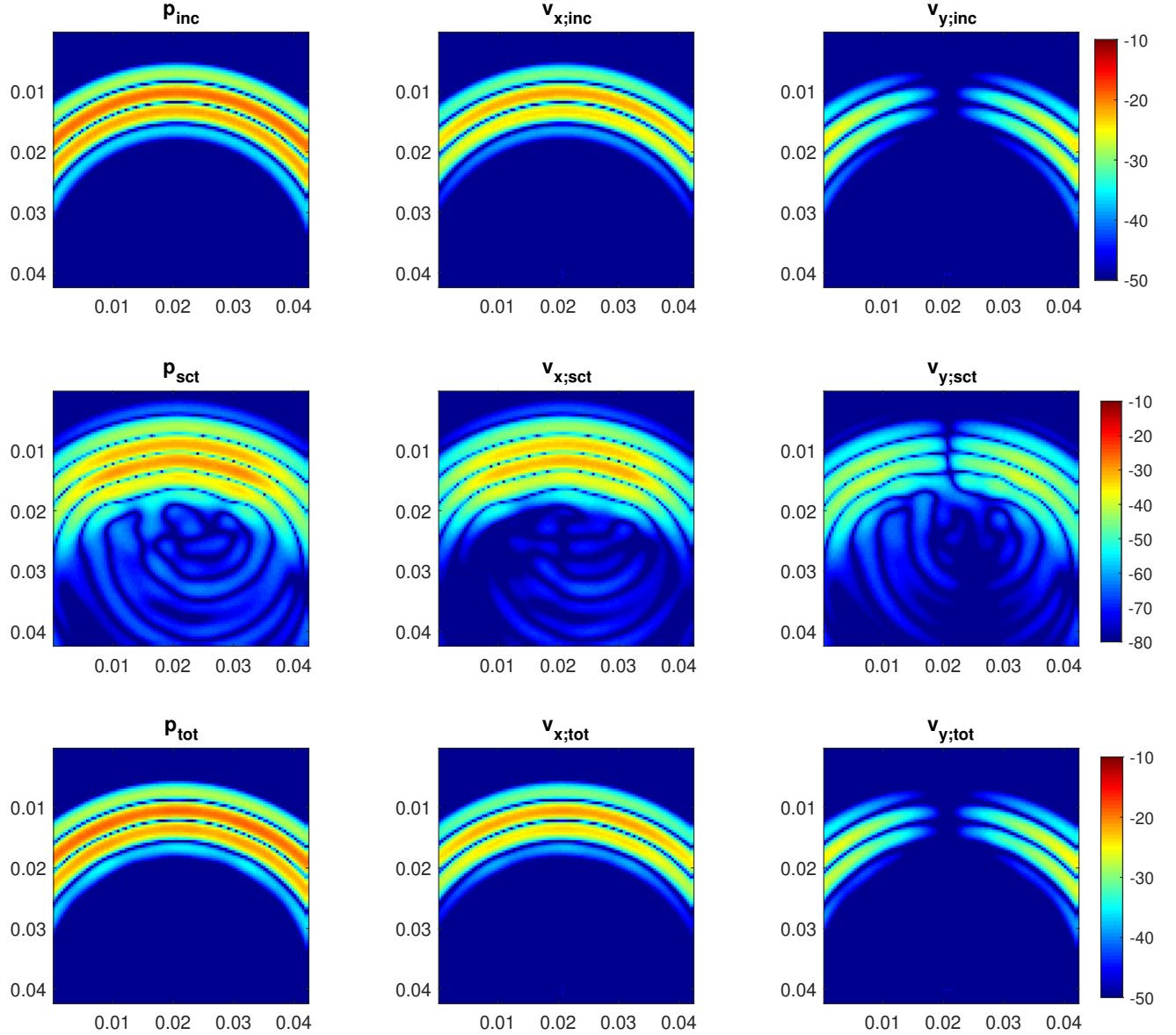


FIG. 4. Snapshots of incident (top row), scattered (middle row) and total fields (bottom row) at $t = 28\mu s$. Left column shows the pressure field; the middle and right columns the particle velocity fields. All fields are normalized with respect to the maximum absolute value and shown on a dB scale.

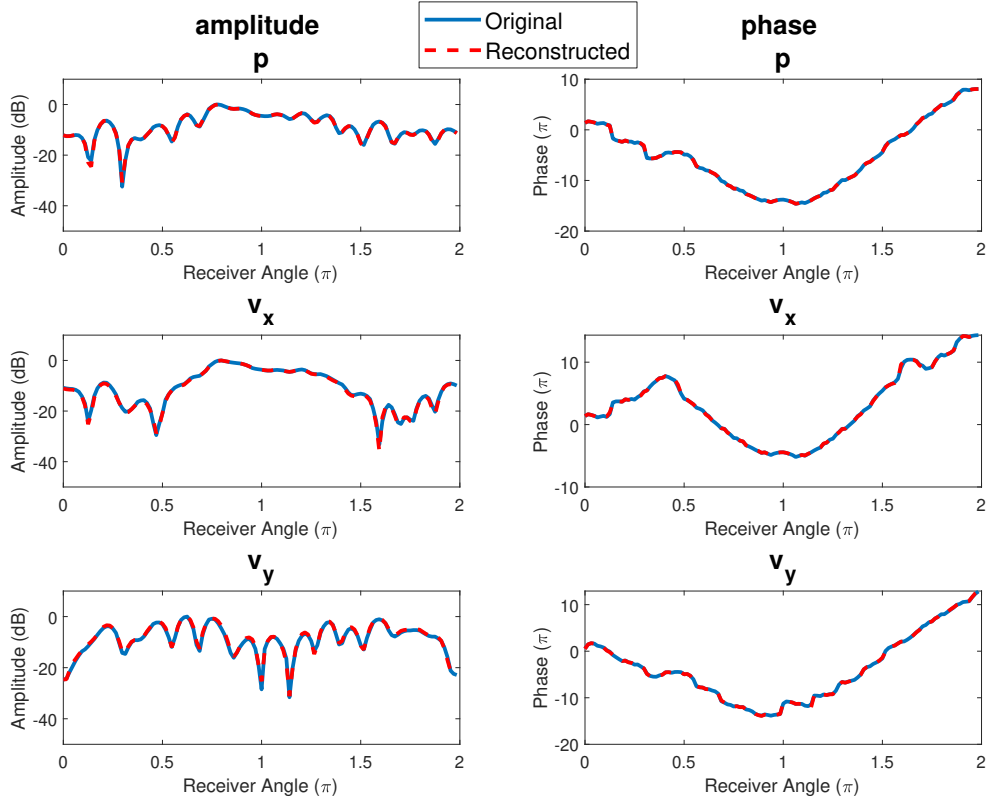


FIG. 5. particle velocity field reconstruction results in frequency domain. Both amplitude (left column) and phase (right column) of the synthetically generated and reconstructed fields are shown. Top row shows the Hankel decomposition of the pressure field (red) with the synthetically generated (blue); middle and bottom row the reconstructed particle velocity fields (red) together with the synthetically generated (blue).

169 together and inverting for both compressibility and density. For all examples, 32 sources
 170 and 128 receivers are used, all equally distributed on a circle with radius $r = 20$ mm, see
 171 Fig. 2. Ten frequency components are used for the inversion, see Fig. 3.

172 Fig. 7 shows the single-parameter inversion results obtained with CSI after 2048 iterations.
 173 The first row shows the true compressibility, density and speed of sound profiles. The second
 174 row shows the inversion results using pressure field only and assuming constant density.

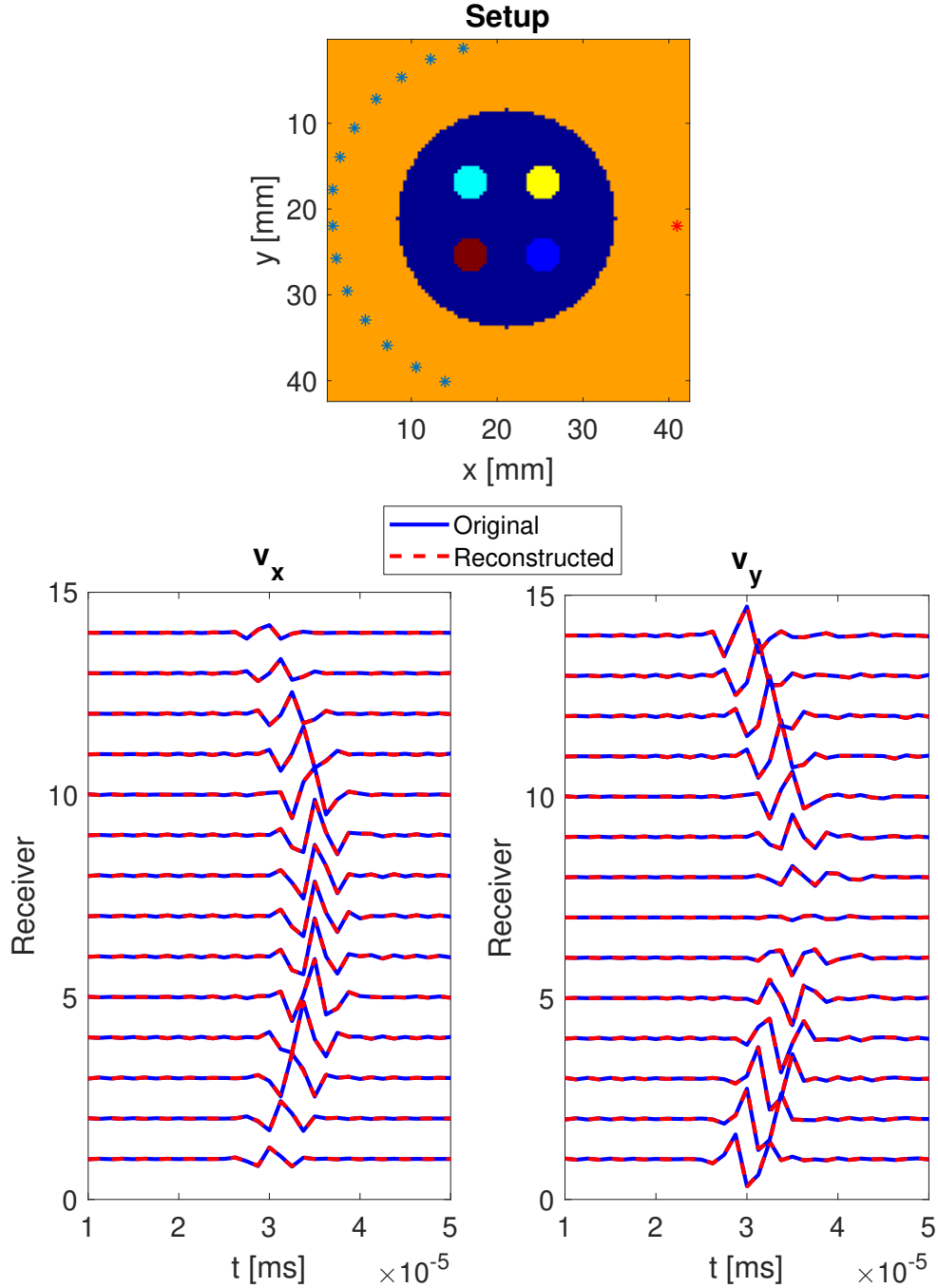


FIG. 6. particle velocity field reconstruction results in time domain. The top image shows the locations of the source (red star) and the 15 receivers (blue stars). The bottom images show the reconstructed particle velocity field (red) together with the ground truth (blue). Note that, all fields are normalized with respect to the maximum value.

175 The four small lesions are all visible in the results but with wrong parameter values. The
176 values for the compressibility and density contrast in the lower right corner are selected
177 such that small cylinder doesn't show any speed of sound contrast with respect to its direct
178 surrounding but that it still will give rise to scattering. Not allowing for a density contrast
179 during reconstruction automatically means the formation of an erroneous speed of sound
180 contrast at this particular location.

181 Note that in literature there are works that show that single-parameter inversion recon-
182 structs speed of sound accurately with experimental data. With this specific example we
183 intended to show where these single-parameter inversion methods might face problems.

184 Fig. 8 shows the multi-parameter inversion results obtained with CSI after 2048 iterations.
185 The first row shows the true compressibility, density and speed of sound profiles. These
186 profiles are identical to the ones used in Fig. 7. The second row shows the inversion results
187 using the synthetically generated pressure and particle velocity fields. The third row shows
188 the inversion results when the synthetically generated pressure and reconstructed particle
189 velocity fields are used to invert for both density and compressibility. In both cases similar
190 results are obtained and the four small lesions have almost the correct parameter values. The
191 ripples seen in the background are caused by the coarse discretization of the domain and can
192 be solved by using a finer spatial discretization or additional regularization based on total
193 variation or sparsity constraints^{21,28}. Integral equation formulations have the advantage that
194 they perform well with relatively coarse sampling because of having a bounded operator.
195 This is valid for CSI for the single-parameter inversion. However, this feature is not valid
196 for the multi-parameter inversion anymore. The operator in multi-parameter inversion is

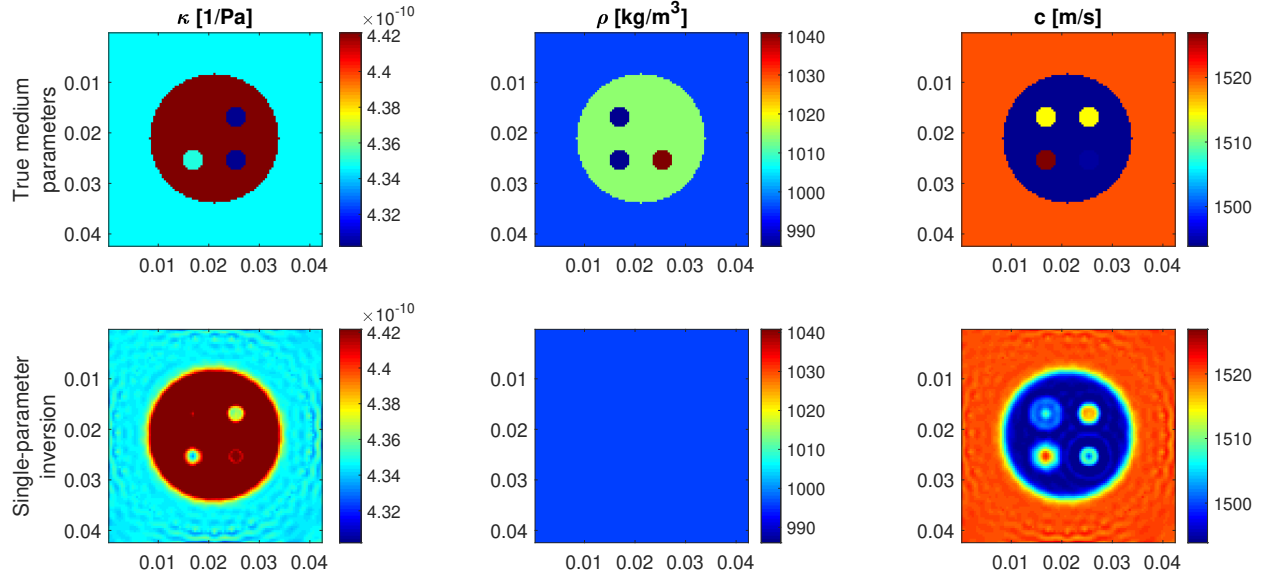


FIG. 7. Contrast source inversion results (single-parameter). Top row shows the true compressibility, density and speed of sound profiles; bottom row shows the CSI reconstruction using the synthetically generated pressure field only and assuming constant density. Note that with this example we intend to show the leakage of density contrast into a compressibility and hence speed of sound contrast.

197 unbounded because of the spatial derivatives. Therefore, a finer discretization would also
 198 improve these results.

199 To examine the performance of the method against noise, we added 5% complex valued
 200 white noise to the data. Results for the reconstructions are shown in Fig. 9. It can be seen
 201 from these results that all small inclusions are reconstructed with a good accuracy.

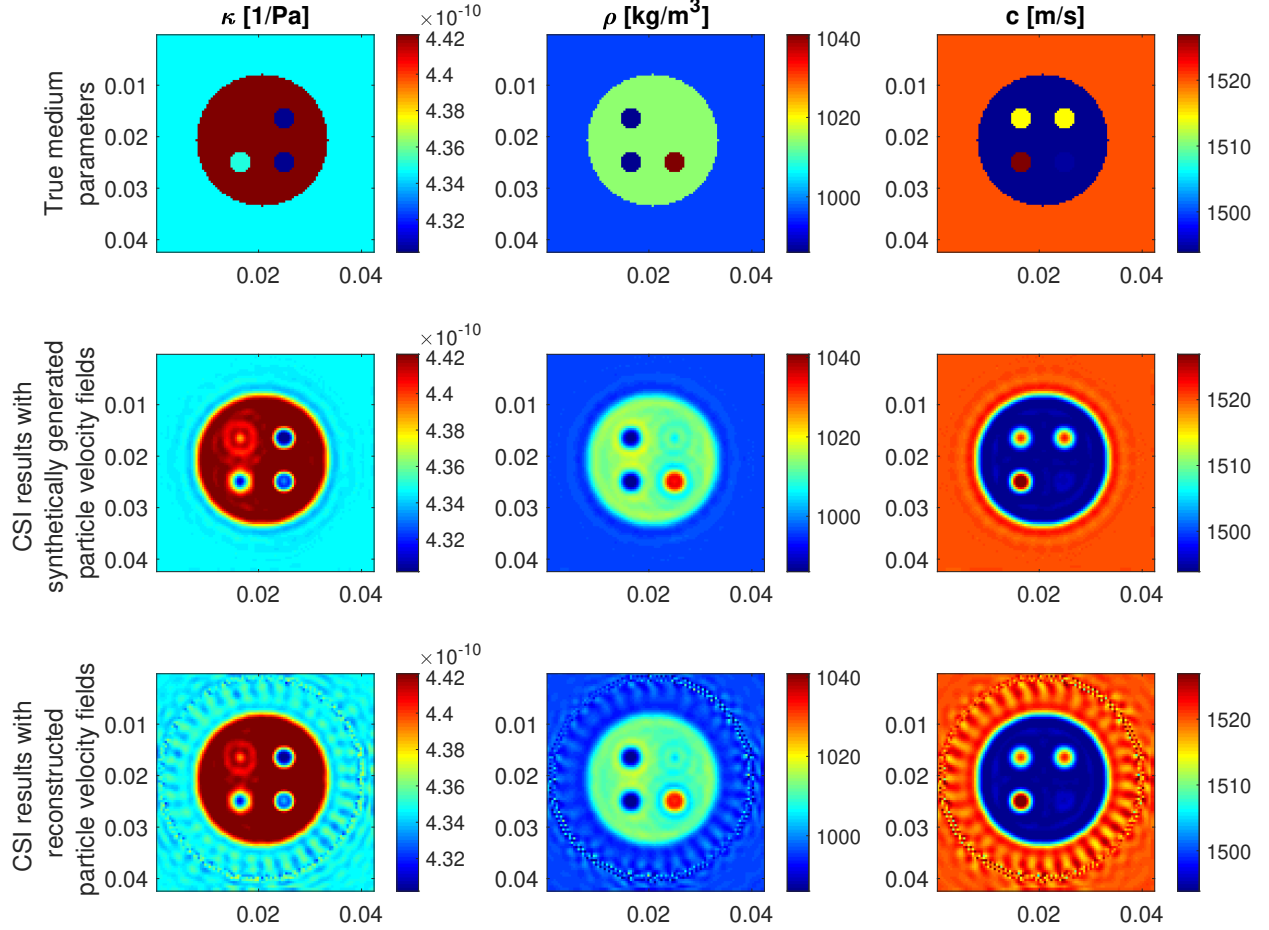


FIG. 8. Contrast source inversion results (multi-parameter). Top row shows the true compressibility, density and speed of sound profiles; middle row shows the CSI reconstruction using synthetically generated pressure and particle velocity fields; bottom row shows the CSI reconstruction using pressure field together with reconstructed particle velocity fields.

202 **IV. CONCLUSION**

203 In this paper, we present a multi-parameter full-wave inversion method where the required
 204 particle velocity field is reconstructed from the measured pressure field using Hankel function
 205 decomposition. The inversion method has been successfully tested using a 2-D synthetic

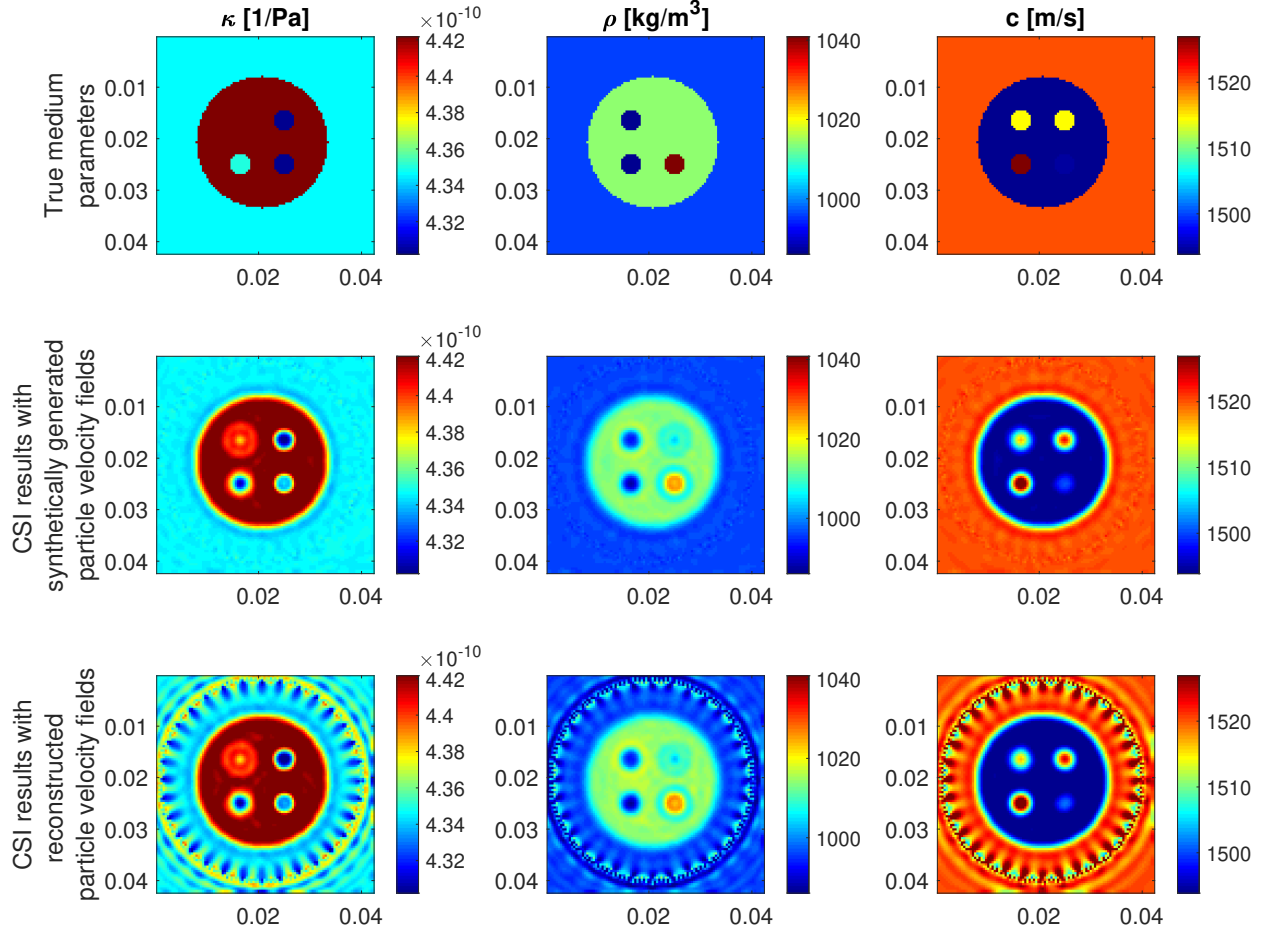


FIG. 9. Same as Fig. 8 but now with 5% noise added to the data.

206 example; a breast phantom containing heterogeneities in compressibility, density and speed
 207 of sound.

208 First we have tested the particle velocity field reconstruction method. To this end, the
 209 particle velocity field obtained by solving the full vectorial forward problem has been com-
 210 pared with the reconstructed particle velocity field using the synthetically measured pressure
 211 field. It has been shown that both particle velocity fields matches each other perfectly well.

212 Next, the synthetically measured pressured field has been used together with the recon-
 213 structed particle velocity field to successfully invert for density, compressibility and speed-of

214 sound profiles using a full-wave inversion method referred to as contrast source inversion
215 (CSI). Finally, CSI has been implemented in its traditional way where only a pressure field
216 is used to invert for a speed of sound profile given the assumption of a constant density.
217 Application of this single-parameter inversion on the synthetic data derived from the multi-
218 parameter synthetic breast phantom gives rise to “ghost” objects in the resulting speed of
219 sound profile. These results underline the importance of multi-parameter inversion in case
220 the object of interest shows spatial variations in compressibility, density and speed of sound.

221 Attenuation is another important parameter in medical ultrasound. There are already
222 quite some inversion related work that includes attenuation. We believe that it needs detailed
223 examination in a future paper. Finally, a 3-D extension of the method introduced in this
224 paper is straightforward and would only lead to an increase in computational load.²⁹

225 **ACKNOWLEDGMENTS**

226 The authors would like to thank Joost van der Neut for his valuable input.

227 **References**

228 ¹N. K. Martiartu, C. Boehm, and A. Fichtner, “3d wave-equation-based finite-frequency
229 tomography for ultrasound computed tomography,” *IEEE Transactions on Ultrasonics,*
230 *Ferroelectrics, and Frequency Control* (2020).

231 ²R. J. Lavarello and M. L. Oelze, “Tomographic reconstruction of three-dimensional vol-
232 umes using the distorted born iterative method,” *IEEE Transactions on Medical Imaging*

233 **28**(10), 1643–1653 (2009).

234 ³H. Gemmeke and N. Ruiter, “3d ultrasound computer tomography for medical imaging,”
235 Nuclear Instruments and Methods in Physics Research Section A: Accelerators, Spectrom-
236 eters, Detectors and Associated Equipment **580**(2), 1057–1065 (2007).

237 ⁴N. Ozmen, R. Dapp, M. Zapf, H. Gemmeke, N. V. Ruiter, and K. W. A. van Dongen,
238 “Comparing different ultrasound imaging methods for breast cancer detection,” IEEE
239 Trans. Ultrason., Ferroelectr., Freq. Control **62**(4), 637–646 (2015).

240 ⁵M. Pérez-Liva, J. Herraiz, J. Udías, E. Miller, B. Cox, and B. Treeby, “Time domain
241 reconstruction of sound speed and attenuation in ultrasound computed tomography using
242 full wave inversion,” The Journal of the Acoustical Society of America **141**(3), 1595–1604
243 (2017).

244 ⁶G. Y. S. Sandhu, C. Li, O. Roy, S. Schmidt, and N. Duric, “High-resolution quantitative
245 whole-breast ultrasound: in vivo application using frequency-domain waveform tomogra-
246 phy,” in *Medical Imaging 2015: Ultrasonic Imaging and Tomography*, International Society
247 for Optics and Photonics (2015), Vol. 9419, p. 94190D.

248 ⁷K. Wang, T. Matthews, F. Anis, C. Li, N. Duric, and M. A. Anastasio, “Waveform inver-
249 sion with source encoding for breast sound speed reconstruction in ultrasound computed
250 tomography,” IEEE transactions on ultrasonics, ferroelectrics, and frequency control **62**(3),
251 475–493 (2015).

252 ⁸N. Duric, P. Littrup, L. Poulo, A. Babkin, R. Pevzner, E. Holsapple, O. Rama, and
253 C. Glide, “Detection of breast cancer with ultrasound tomography: First results with the

254 computed ultrasound risk evaluation (cure) prototype,” *Medical physics* **34**(2), 773–785
255 (2007).

256 ⁹L. Guasch, O. C. Agudo, M.-X. Tang, P. Nachev, and M. Warner, “Full-waveform inversion
257 imaging of the human brain,” *NPJ Digital Medicine* **3**(1), 1–12 (2020).

258 ¹⁰S. Bernard, V. Monteiller, D. Komatitsch, and P. Lasaygues, “Ultrasonic computed to-
259 mography based on full-waveform inversion for bone quantitative imaging,” *Physics in*
260 *Medicine & Biology* **62**(17), 7011 (2017).

261 ¹¹B. Malik, J. Klock, J. Wiskin, and M. Lenox, “Objective breast tissue image classifica-
262 tion using quantitative transmission ultrasound tomography,” *Scientific reports* **6**, 38857
263 (2016).

264 ¹²X. Song, M. Li, F. Yang, S. Xu, and A. Abubakar, “Feasibility study of acoustic imaging
265 for human thorax using an acoustic contrast source inversion algorithm,” *The Journal of*
266 *the Acoustical Society of America* **144**(5), 2782–2792 (2018).

267 ¹³P. Mojabi and J. LoVetri, “Ultrasound tomography for simultaneous reconstruction of
268 acoustic density, attenuation, and compressibility profiles,” *The Journal of the Acoustical*
269 *Society of America* **137**(4), 1813–1825 (2015).

270 ¹⁴P. Mojabi and J. LoVetri, “Evaluation of balanced ultrasound breast imaging under three
271 density profile assumptions,” *IEEE Transactions on Computational Imaging* **3**(4), 864–875
272 (2017).

273 ¹⁵K. W. A. van Dongen and W. M. Wright, “A full vectorial contrast source inversion scheme
274 for three-dimensional acoustic imaging of both compressibility and density profiles,” *The*

- 275 Journal of the Acoustical Society of America **121**(3), 1538–1549 (2007).
- 276 ¹⁶U. Taskin, J. van der Neut, H. Gemmeke, and K. W. A. van Dongen, “Redatuming of
277 2-d wave fields measured on an arbitrary-shaped closed aperture,” IEEE transactions on
278 ultrasonics, ferroelectrics, and frequency control **67**(1), 173–179 (2019).
- 279 ¹⁷A. De Hoop, “Handbook of radiation and scattering of waves: Acoustic waves in flu-
280 ids, elastic waves in solids, electromagnetic waves: with corrections,” Former publisher:
281 Academic Press (2008).
- 282 ¹⁸J. T. Fokkema and P. M. van den Berg, *Seismic applications of acoustic reciprocity* (Else-
283 vier, 2013).
- 284 ¹⁹F. B. Jensen, W. A. Kuperman, M. B. Porter, and H. Schmidt, *Computational ocean*
285 *acoustics* (Springer Science & Business Media, 2011).
- 286 ²⁰M. Abramowitz, “Abramowitz and stegun: Handbook of mathematical functions,” US
287 Department of Commerce **10** (1972).
- 288 ²¹A. B. Ramirez and K. W. A. van Dongen, “Sparsity constrained contrast source inversion,”
289 The Journal of the Acoustical Society of America **140**(3), 1749–1757 (2016).
- 290 ²²K. W. A. van Dongen and W. M. Wright, “A forward model and conjugate gradient
291 inversion technique for low-frequency ultrasonic imaging,” The Journal of the Acoustical
292 Society of America **120**(4), 2086–2095 (2006).
- 293 ²³T. L. Szabo, *Diagnostic ultrasound imaging: inside out* (Academic Press, 2004).
- 294 ²⁴F. A. Duck, *Physical properties of tissues: a comprehensive reference book* (Academic
295 press, 2013).

- 296 ²⁵U. Taskin, N. Ozmen, H. Gemmeke, and K. W. A. van Dongen, “Modeling breast ul-
297 trasound; on the applicability of commonly made approximations,” *Archives of Acoustics*
298 **43**(3) (2018).
- 299 ²⁶A. B. Ramirez, S. A. Abreo, and K. W. A. van Dongen, “Selecting the number and location
300 of sources and receivers for non-linear time-domain inversion,” in *2017 IEEE International*
301 *Ultrasonics Symposium (IUS)*, IEEE (2017), pp. 1–3.
- 302 ²⁷P. M. van den Berg and A. Abubakar, “Contrast source inversion method: State of art,”
303 *Progress in Electromagnetic Research* **34**, 189–218 (2001).
- 304 ²⁸A. Abubakar and P. M. Van Den Berg, “Total variation as a multiplicative constraint
305 for solving inverse problems,” *IEEE Transactions on Image Processing* **10**(9), 1384–1392
306 (2001).
- 307 ²⁹U. Taskin and K. W. A. van Dongen, “3-d redatuming for breast ultrasound,” in *Medical*
308 *Imaging 2020: Physics of Medical Imaging*, International Society for Optics and Photonics
309 (2020), Vol. 11312, p. 113125H.